CrossMark

J. Fluid Mech. (2014), *vol.* 759, *pp.* 739–750. © Cambridge University Press 2014
doi:10.1017/jfm.2014.550

Finite-size effects in parametric subharmonic instability

Baptiste Bourget[1], Hélène Scolan[1], Thierry Dauxois[1], Michael Le Bars[2], Philippe Odier[1] and Sylvain Joubaud[1,†]

[1]Laboratoire de Physique de l'École Normale Supérieure de Lyon, Université de Lyon, CNRS, 46 Allée d'Italie, F-69364 Lyon CEDEX 07, France

[2]CNRS, Aix-Marseille Université, Ecole Centrale Marseille, IRPHE UMR 7342, 49 rue F. Joliot-Curie, 13013 Marseille, France

(Received 28 February 2014; revised 16 September 2014; accepted 17 September 2014; first published online 28 October 2014)

The parametric subharmonic instability (PSI) in stratified fluids depends on the frequency and the amplitude of the primary plane wave. In this paper, we present experimental and numerical results emphasizing that the finite width of the beam also plays an important role on this triadic instability. A new theoretical approach based on a simple energy balance is developed and compared with numerical and experimental results. Owing to the finite width of the primary wave beam, the secondary pair of waves can leave the interaction zone which affects the transfer of energy. Experimental and numerical results are in good agreement with the prediction of this theory, which brings new insights on energy transfers in the ocean where internal waves with finite-width beams are dominant.

Key words: geophysical and geological flows, internal waves, parametric instability

1. Introduction

Nonlinear resonant interaction of internal waves is one of the key processes leading to small-scale mixing in the ocean. In particular, the parametric subharmonic instability (PSI) allows the transport of energy from large to smaller scales by giving birth to two secondary subharmonic waves (with wavevector modulus κ_1 and κ_2) from an initial primary wave (with wavevector modulus κ_0) (Benielli & Sommeria 1998; Koudella & Staquet 2006; Clark & Sutherland 2010; Bourget *et al.* 2013; Gayen & Sarkar 2013). Thanks to a new experimental and analysis tool, Bourget *et al.* (2013) have recently shown how the PSI theory developed for plane waves is in good agreement with the experimental observations of the instability of a quasi-monochromatic wave beam. As stressed by Sutherland (2013), one challenge is now to determine the range of validity of the theory and in particular the role of the width of the wave beam on the occurrence of the instability. In other words, is the instability affected by the width of the beam? This question is particularly important in the oceanic context where internal waves are known to develop preferentially in the form of finite size beams, for instance waves emitted by the interaction of tide with

†Email address for correspondence: Sylvain.Joubaud@ens-lyon.fr

https://doi.org/10.1017/jfm.2014.550 Published online by Cambridge University Press

Configuration	N (rad s^{-1})	ω_0/N	ℓ_0 (m^{-1})	Ψ_0/ν	W	Approach
I	0.89	0.85	110	16.9	$1–5\lambda_0$	Experimental
II	0.89	0.85	110	16.9	$2–3\lambda_0$	Numerical
III	0.91	0.74	75	33	$3\lambda_0$	Experimental
IV	0.91	0.74	75	33	$3\lambda_0$	Numerical
V	0.91	0.74	75	33	$20\lambda_0$	Numerical

TABLE 1. Experimental and numerical parameters, with N the buoyancy frequency, ω_0 the frequency of the primary wave, λ_0 the wavelength, ℓ_0 the horizontal wavenumber, $\Psi_0 = v_0/\ell_0$ the experimentally measured amplitude of the stream function in which v_0 is the vertical velocity, ν the viscosity and W the width of the primary beam.

topography (Dewan *et al.* 1998; Lien & Gregg 2001; Gostiaux & Dauxois 2007). Moreover, energy transfer between scales, as well as wave turbulence in oceans, are open questions and a study of the role of the beam width on secondary waves selection in PSI might bring new understanding to these issues.

This is the aim of the present work, combining experimental, numerical and theoretical approaches. Starting with the observation that finite-width beams can inhibit the instability, we continue by studying the effect of the beam width on the selection rules.

2. Experimental and numerical approach

2.1. *Experimental set-up*

A tank 160 cm large, 17 cm wide is filled with 36 cm of linearly stratified salt water with constant buoyancy frequency N. An internal wave of wavelength λ_0 is generated using a wave generator (Gostiaux *et al.* 2007; Mercier *et al.* 2010) placed horizontally with a plane wave configuration identical to that used by Bourget *et al.* (2013). Note that to avoid spurious emission of internal waves on the extremities of the moving region, the amplitude of the plates is constant over n wavelengths in the central region, while one half-wavelength with a smooth decrease of the amplitude is added on each side. The beam width $W = (n+1)\lambda_0$ is varied from λ_0 to $5\lambda_0$ by changing the horizontal extent of the moving part of the wavemaker. A schematic view of the experimental set-up is shown in figure 1. A synthetic schlieren technique (Sutherland *et al.* 1999; Dalziel, Hughes & Sutherland 2000) is used to obtain the two-dimensional instantaneous density gradient field ($\tilde{\rho}_x(x, z, t) = \partial_x(\rho(x, z, t) - \rho_0(z))$, $\tilde{\rho}_z(x, z, t) = \partial_z(\rho(x, z, t) - \rho_0(z))$) where $\rho(x, z, t)$ and $\rho_0(z)$ are the instantaneous and initial fluid densities. Series of experiments are performed varying the horizontal wavenumber ℓ_0, the plate motion amplitude a and the frequency ω_0. It results in variations of the vertical wavenumber m_0 according to the dispersion relation $\omega_0/N = \ell_0/\kappa_0$, as well as variations of Ψ_0, the amplitude of the stream function ψ, which is defined such that $\partial_z\psi = -u$ and $\partial_x\psi = v$ with u and v the horizontal and vertical components of the velocity. The parameters used in this article are summarized in table 1. A typical experimental result is presented as background of figure 1.

2.2. *Numerical method*

In addition to the experiments, we performed 2D direct numerical simulations with the finite-elements commercial software Comsol Multiphysics. The simulations solve

https://doi.org/10.1017/jfm.2014.550 Published online by Cambridge University Press

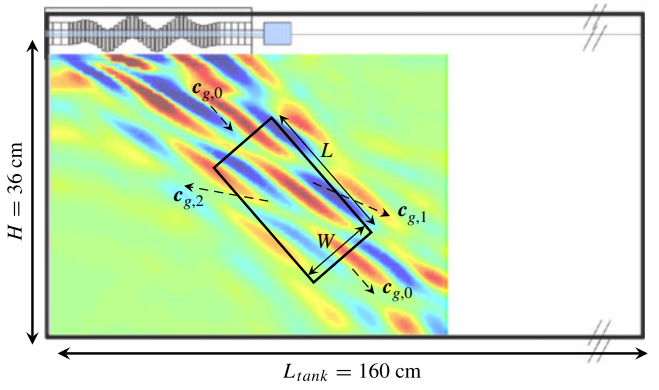


FIGURE 1. (Colour online) Sketch of the set-up. Experimentally, the wave generator is lying horizontally at the top of the wave tank. The vertical density gradient field of a typical wave beam generated at the top of the domain and undergoing PSI is presented as background of the figure. The dashed arrows indicate the group velocity of the three wave beams. The tilted rectangle of length L and width W corresponds to the control area used in the model.

the incompressible continuity equation, the Navier–Stokes equations for a Newtonian fluid in the Boussinesq approximation and the equation of salinity conservation. All elements are triangular standard Lagrange mesh of type P_2–P_3 (i.e. quadratic for the pressure field but cubic for the velocity and density fields). The total number of degrees of freedom is larger than 2 million. At each time step, the system is solved with the backward difference formulae (BDF) temporal solver and the sparse direct linear solver PARDISO. The Comsol BDF solver automatically adapts its scheme order between 1 and 5 (see the details in Hindmarsh *et al.* 2005): it varies between 1 and 3 during our calculations. Note that no stabilization technique has been used. The Schmidt number, which compares diffusivity of salt and momentum is set to $Sc = 10$ as a proxy for the value $Sc = 700$ existing in the laboratory configuration. To prevent the creation of a reflected beam at the bottom of the domain, an attenuation layer is added wherein viscosity and diffusivity of salt increase exponentially with depth. To mimic the wavemaker of the experimental set-up, the horizontal velocity, the vertical velocity and the density are simultaneously imposed at each time step at the top horizontal boundary and correspond to linear gravity waves. The amplitude of the imposed velocities and density is constant over n wavelengths in the central region, while one half-wavelength with a smooth decrease of the amplitude is added on each side similar to the experimental configuration. On the left and the bottom of the domain, we impose no stress and no flux and on the right, the pressure anomaly is fixed to zero, with no viscous stress and flux. Note that at time $t = 0$, the linear viscous beam is imposed in the bulk. The advantage of the numerical approach is that the beam width can be varied to much larger value than five wavelengths.

2.3. *Results*

Let us first focus on the experimental and numerical results of configurations I and II. Figures 2(*a*) and 2(*c*) present the time evolution of the vertical density gradients measured at a given point in the experiment (configuration I), while figures 2(*b*) and 2(*d*) show the same information for the numerical simulation (configuration II).

https://doi.org/10.1017/jfm.2014.550 Published online by Cambridge University Press

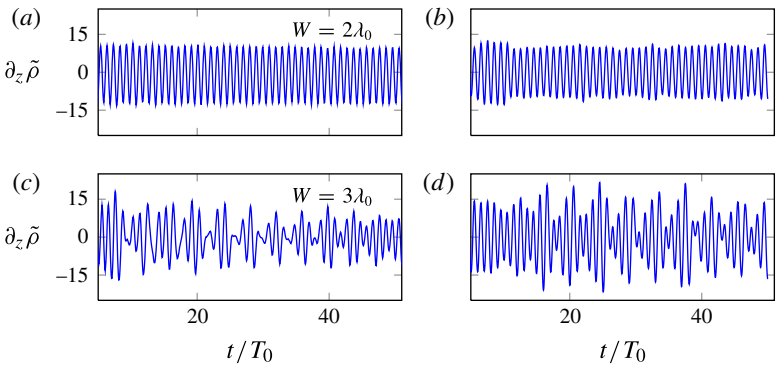


FIGURE 2. (Colour online) Time evolution of the amplitude of $\partial_z\tilde{\rho}$ (kg m^{-4}) 4.5 cm below the wavemaker and in the middle of the beam as the width of the beam is increased from $W = 2\lambda_0$ (a,b) to $3\lambda_0$ (c,d) for configurations I–II ($\omega_0/N = 0.85$, $\ell_0 = 110$ m^{-1}, $\psi_0/\nu = 16.9$). Experimental results are shown in (a,c) and numerical results in (b,d).

Configuration	W (rad s^{-1})	ω_1/N	κ_1 (m^{-1})	ω_2/N	κ_2 (m^{-1})	Approach
I	3–5 λ_0	0.64	220	0.25	120	Experimental
II	$3\lambda_0$	0.60	201	0.26	101	Numerical
III	$3\lambda_0$	0.49	208	0.26	121	Experimental
IV	$3\lambda_0$	0.49	232	0.25	148	Numerical
V	$20\lambda_0$	0.50	147	0.27	61	Numerical

TABLE 2. Experimental and numerical values of ω_1 and ω_2, the frequencies of the secondary waves and κ_1 and κ_2, the wavevector modulus of the secondary waves.

Experimental and numerical results display a good agreement, evidencing the following observation: while for a beam width $W = 2\lambda_0$ (figure 2a,b), the regular signal does not show any triadic resonance, in the case where $W = 3\lambda_0$ (figure 2c,d), the instability develops, as emphasized by the modulation of the signal, typical of the apparition of new frequencies in the system. Moreover, frequencies and wavelengths of the secondary waves present a good agreement, as can be seen in table 2. For experiments with $W = 4\lambda_0$ and $5\lambda_0$ (not shown), the instability is observed as well. Experimental and numerical results thus reveal for the first time the critical role of the beam width in the occurrence of the triadic instability.

3. Theory

To understand this observation, it is crucial to realize that the theory of PSI is derived for infinitely extended plane waves, as described by Koudella & Staquet (2006) and Bourget *et al.* (2013). We thus propose to take into account the width of the primary wave beam, the guiding idea being that the two secondary plane waves can exit the spatial extent of the primary wave beam (McEwan & Plumb 1977; Gerkema, Staquet & Bouruet-Aubertot 2006). Once they have left this region, they cannot interact any more with the primary plane wave and the energy transfer is broken.

To perform an energy balance, let us define a control area within the primary wave beam as presented by the tilted rectangle in figure 1. For simplicity, we neglect the

https://doi.org/10.1017/jfm.2014.550 Published online by Cambridge University Press

spatial attenuation of the waves in this area, i.e. the surface energy densities E_0, E_1 and E_2 of the different waves are considered uniform. Consequently, the temporal variation of the primary plane wave energy in the domain is due to:

(i) nonlinear interactions that transfer energy from the primary wave to both secondary waves (denoted $\Gamma_{int}(i,j)$ where i and j represent the two other waves of the triad);
(ii) viscosity;
(iii) incoming and outgoing flux of the primary wave.

For the domain $W \times L$, this can be summarized as

$$\frac{\mathrm{d}E_0}{\mathrm{d}t}LW = \Gamma_{int}(1,2) - \nu\kappa_0^2 E_0 LW + E_{in}W\boldsymbol{c}_{g,0} - E_0 W\boldsymbol{c}_{g,0}, \tag{3.1}$$

with E_{in} the surface energy injected by the generator and $c_{g,0} = (N^2 - \omega_0^2)^{1/2}/\kappa_0$.

Assuming that PSI occurs everywhere in the beam, the outgoing energy flux of the secondary waves through the cross-beam faces with width W is compensated by the incoming one. In contrast, since they do not propagate parallel to the primary beam, they exit the control area also from the lateral boundaries without compensation. For the temporal variation of the secondary waves energy in the domain, this leads to

$$\frac{\mathrm{d}E_i}{\mathrm{d}t}LW = \Gamma_{int}(0,j) - \nu\kappa_i^2 E_i LW - E_i L|\boldsymbol{c}_{g,i}\cdot\boldsymbol{e}_{k_0}|, \tag{3.2}$$

with $i = 1, 2$, $j = 2, 1$ and the modulus of the group velocity $c_{g,i} = (N^2 - \omega_i^2)^{1/2}/\kappa_i$.

The first term represents the interaction with the other plane waves of the triadic resonance while the third one accounts for the energy exiting the control area. As $E_i \propto \kappa_i^2 \Psi_i \Psi_i^*$, using the infinite width expression (Bourget *et al.* 2013) for the interaction terms, one obtains

$$\frac{\mathrm{d}\Psi_0}{\mathrm{d}t} = -|I_0|\Psi_1\Psi_2 - \frac{\nu}{2}\kappa_0^2\Psi_0 + F, \tag{3.3}$$

$$\frac{\mathrm{d}\Psi_1}{\mathrm{d}t} = +|I_1|\Psi_0\Psi_2^* - \left(\frac{\nu}{2}\kappa_1^2 + \frac{|\boldsymbol{c}_{g,1}\cdot\boldsymbol{e}_{k_0}|}{2W}\right)\Psi_1, \tag{3.4}$$

$$\frac{\mathrm{d}\Psi_2}{\mathrm{d}t} = +|I_2|\Psi_0\Psi_1^* - \left(\frac{\nu}{2}\kappa_2^2 + \frac{|\boldsymbol{c}_{g,2}\cdot\boldsymbol{e}_{k_0}|}{2W}\right)\Psi_2, \tag{3.5}$$

with I_i the interaction term defined as follows

$$I_i = \frac{\ell_j m_r - m_j \ell_r}{2\omega_i \kappa_i^2}\left[\omega_i(\kappa_j^2 - \kappa_r^2) + \ell_i N^2\left(\frac{\ell_j}{\omega_j} - \frac{\ell_r}{\omega_r}\right)\right] \tag{3.6}$$

with $i, j, r = 0, 1, 2$ and $F = \boldsymbol{c}_{g,0}(\Psi_{in}^*\Psi_{in} - \Psi_0^*\Psi_0)/(2L\Psi_0^*)$ a forcing term, corresponding to the difference between the incoming energy and the outgoing one for the primary wave.

The solution for Ψ_1 and Ψ_2 can be easily obtained with the hypothesis Ψ_0 constant. One finds exponentially growing solutions with growth rate

$$\sigma_\pm = -\tfrac{1}{4}(\Sigma_1 + \Sigma_2) \pm \sqrt{\tfrac{1}{16}(\Sigma_1 - \Sigma_2)^2 + |I_1|\,|I_2|\,|\Psi_0|^2}, \tag{3.7}$$

where $\Sigma_i = \nu\kappa_i^2 + \sigma_{adv}(\kappa_i)$ and $\sigma_{adv}(\kappa_i) = |\boldsymbol{c}_{g,i}\cdot\boldsymbol{e}_{k_0}|/W$, the inverse of an advection time since it characterizes the transport of the secondary waves energy out of the interaction region. The viscous part of the expression of Σ_i is similar to the expression obtained by McEwan & Plumb (1977) in the limit of large Prandtl number.

https://doi.org/10.1017/jfm.2014.550 Published online by Cambridge University Press

Cases with large σ_{adv} values will present a very strong finite-width effect. Three parameters impact the value of the growth rate.

(*a*) The width W of the beam. The term σ_{adv} varies like the inverse of W, thus the growth rate is decreased when the beam is narrow. In contrast, when W goes to infinity, σ_{adv} vanishes and the growth rate of the original theory (Bourget *et al.* 2013) is recovered.

(*b*) The amplitude of the group velocities of the secondary waves. When the modulus of the secondary wavevector κ_i is small, the group velocity increases and the secondary waves exit the primary wave beam more rapidly. So there is less time for them to grow in amplitude. In addition, σ_{adv} is weaker for low stratification N (small group velocity) at κ and ω fixed, which implies a stronger instability in the oceans where N is weak compared with laboratory conditions.

(*c*) The direction of the group velocity of each wave of the triad. When the secondary waves are almost perpendicular to the primary plane wave, they leave the interaction area quickly, which does not favour the instability. To summarize, this finite-width effect is stronger when the group velocity of the secondary wave is aligned with $\boldsymbol{k_0}$.

For configurations I and II presented in figure 2, the above model predicts that the growth rate is an increasing function of W. For an infinitely wide wave beam, the instability occurs for any value of the amplitude (see appendix A). In contrast, for finite-width beams, a non-vanishing threshold appears. For example, for $W = 2\lambda_0$, the maximum growth rate becomes negative for $\Psi_0/\nu < 4.4$. Moreover, during the finite duration of the experiment, even if the instability occurs, the amplitude of the two secondary waves might be too small to be detected. For example, we can define a detection criterion by requiring that for the secondary waves to be detected, the duration of the experiment must exceed three times the inverse of the growth rate. With this criterion, in the case of an infinitely wide wave beam, the instability can only be observed during the experiment if $\Psi_0/\nu > 1.6$ whereas for $W = 2\lambda_0$, the threshold is five times higher, $\Psi_0/\nu > 8.5$. Interestingly, this value of amplitude threshold has the same order of magnitude as the imposed amplitude in configurations I and II, notwithstanding the simplifying hypothesis made by neglecting spatial attenuation in the longitudinal (viscous decay) and transversal (imposed wave beam shape) direction of the primary wave. Therefore, the above model gives an explanation why the instability occurs in these two configurations only for W larger than $3\lambda_0$.

This new analysis reveals a dramatic effect on the development of the triad instability which has been totally overlooked before. When the beam gets narrower, the PSI cut-off, initially due only to viscosity, is displaced towards a larger forcing amplitude so that at a given amplitude, the instability can be completely suppressed by decreasing the beam width.

4. Selection of the triad

We will now show that the finite-width effect can also result in a specific triad selection. To do that, we focus on the results for another set of parameters (configurations III–V, see table 1), this case is therefore different from the previous one. Experimental and numerical wavefields (respectively, configurations III and IV) presented in figure 3(*a*,*b*) are in good agreement. As underlined by Bourget *et al.* (2013), the theoretical prediction for an infinite primary plane wave is that for this

https://doi.org/10.1017/jfm.2014.550 Published online by Cambridge University Press

set of parameters (configurations III–IV), the wavelength of one of the secondary waves generated by the instability is larger than the primary wavelength, while the other one is smaller (see table 2). In this case, the energetic transfer will occur towards larger and smaller scales simultaneously. However, this prediction was not verified and a different type of triad was observed experimentally in Bourget *et al.* (2013), with transfer to smaller scales only. This difference between the prediction and the observations can again be traced back to the finite width of the wave beam. To demonstrate that, we rely on numerical results since the experimental set-up cannot generate plane waves with a beam size larger than $6\lambda_0$. Note that we have performed numerical simulations for $6\lambda_0$ (yielding similar results as for $3\lambda_0$) and $10\lambda_0$ (yielding similar results as for $20\lambda_0$). Therefore, we do not show these results here and focus only on the extreme cases $3\lambda_0$ and $20\lambda_0$. Figure 3(*c*) shows the results of configuration V, i.e. for the same parameters but for a significantly wider beam ($20\lambda_0$). The primary wave beam is still unstable, but the secondary waves look quite different compared with the results for $W = 3\lambda_0$. To quantify the differences, a temporal Hilbert transform (Mercier, Garnier & Dauxois 2008) and a spatial Fourier transform are used to measure the different wavevectors present in the numerical density gradient fields. These vectors are shown in figure 4(*a*,*b*). In addition, the curves in these figures represent the location of the tip of all possible wavevectors $\boldsymbol{k}_1$ satisfying the theoretical resonance conditions with a growth rate possessing a positive real part. A clear difference between the two cases is visible. For $W = 3\lambda_0$, a single triad is observed and its secondary wavevectors $\boldsymbol{k}_1$ belongs to an external branch of the theoretical resonance loci ($\ell_1 > \ell_0$). The wavelengths of both secondary waves are smaller than the primary wavelength. For $W = 20\lambda_0$, two different triads are measured. The first (dashed vectors), with secondary vector $\boldsymbol{k}_{1,e}$ lying on an external branch (hence, the subscript 'e'), is similar to that found for smaller W. For the second (solid vectors), its secondary vector $\boldsymbol{k}_{1,c}$ is located in the central region of the theoretical loci curve ($0 < \ell_1 < \ell_0$). In this case, one secondary wave has a larger wavelength than the primary wave and the other a smaller one.

These observations can be explained by the finite-width theoretical approach presented previously: the predicted evolution of the maximum value of the growth rate as a function of W is shown in figure 4(*c*). The growth rates were computed separately for the external ($\circ$ symbols) and central ($+$ symbols) cases. A transition between the two possible triads is predicted around $W_c = 7\lambda_0$. For $W < W_c$, the most unstable triad is on the external branch. The corresponding predicted location of the tip of wavevector $\boldsymbol{k}_1$ is displayed as a rectangle in figure 4(*a*), showing a very good agreement with the numerical observation. For this narrow beam, this agreement extends as well to the experimental data. In contrast, for wide enough beams, i.e. above the threshold W_c, in spite of the fact that $\boldsymbol{k}_{1,c}$ is almost perpendicular to $\boldsymbol{k}_0$ (a condition enhancing the value of σ_{adv}), the secondary waves have time to grow before leaving the interaction area. Consequently, the central triad becomes dominant when increasing the beam width. In the time evolution of the numerical experiment, this triad appears first, the result derived for infinitely wide beams is thus recovered. At a later time, it is followed by the second triad. Our numerical results confirm that the width of the beam changes the selection of the triad. This new effect explains why energy transfer is mainly towards smaller scales for narrow beams.

5. Oceanic case

This new finite-width theory is therefore of importance when considering internal wave beams from *in situ* observations of the ocean (Dewan *et al.* 1998; Lien & Gregg 2001; Gostiaux & Dauxois 2007). In the ocean, since the wavelengths

https://doi.org/10.1017/jfm.2014.550 Published online by Cambridge University Press

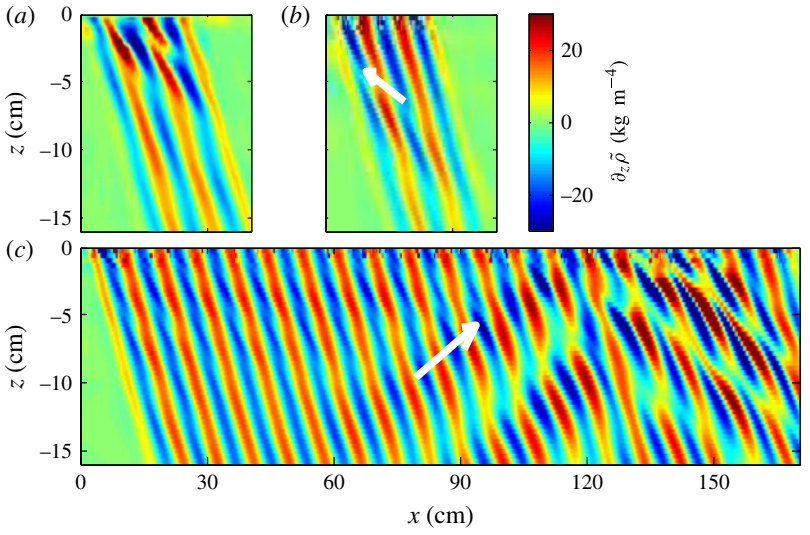


FIGURE 3. (Colour online) Vertical density gradient fields for configurations III–V ($\omega_0/N = 0.74$, $\ell_0 = 75$ m^{-1}, $\psi_0/\nu = 33$): (*a*) experiments with $W = 3\lambda_0$; (*b*) simulations with $W = 3\lambda_0$; (*c*) simulations with $W = 20\lambda_0$. The two vectors represent the direction of the group velocity for one of the two secondary plane waves.

are larger by several orders of magnitude, the Reynolds number is much larger than in the experiments and consequently viscous effects can be safely neglected. Consequently, the beam width is the dominating control parameter for the growth rate. We will focus on equatorial regions, for which the background rotation has no effect.

For example, we consider a primary beam with the following typical parameters:

(*a*) $\omega_0 = 1.4 \times 10^{-4}$ rad s^{-1}, which corresponds to the diurnal M2 tide period;
(*b*) $\lambda_0 = 100$ m, which corresponds to field measurements in Kaena Ridge, Hawaii (Sun & Pinkel 2013);
(*c*) $N = 1.12 \times 10^{-3}$ rad s^{-1}; this value of the buoyancy frequency allows a propagation angle of $\theta = 7°$ which is close to oceanic observations;
(*d*) the Froude number $Fr = u_0 m_0/(2\pi N) = 0.035$ (Gayen & Sarkar 2013) which allows us to estimate Ψ_0;
(*e*) the vertical component of the Coriolis force is ignored and the Coriolis parameter f is set to zero.

Figure 5(*a*) shows the evolution of the growth rate as a function of the width of the beam. With the chosen parameters, the transition between the external and central triad configurations is obtained around $W = 1.5\lambda_0$. Figure 5(*b*) presents the evolution of the modulus of the secondary wavevectors for the external case (black lines) and the central case (grey lines) as a function of the width of the primary beam. For example for a narrow beam $W = 1\lambda_0$, the maximum of growth rate is obtained on the external branch (5*a*) and PSI enables a transfer to smaller scales: $\kappa_1 = 12\kappa_0$, $\kappa_2 = 11\kappa_0$ (figure 5*b*). This behaviour corresponds to simulations (Gerkema *et al.* 2006; Gayen & Sarkar 2013) and to oceanic observations (McKinnon *et al.* 2012). Moreover, the value of the growth rate predicted by the model ($\sigma = 1.2$ day^{-1}) gives a value which has the

https://doi.org/10.1017/jfm.2014.550 Published online by Cambridge University Press

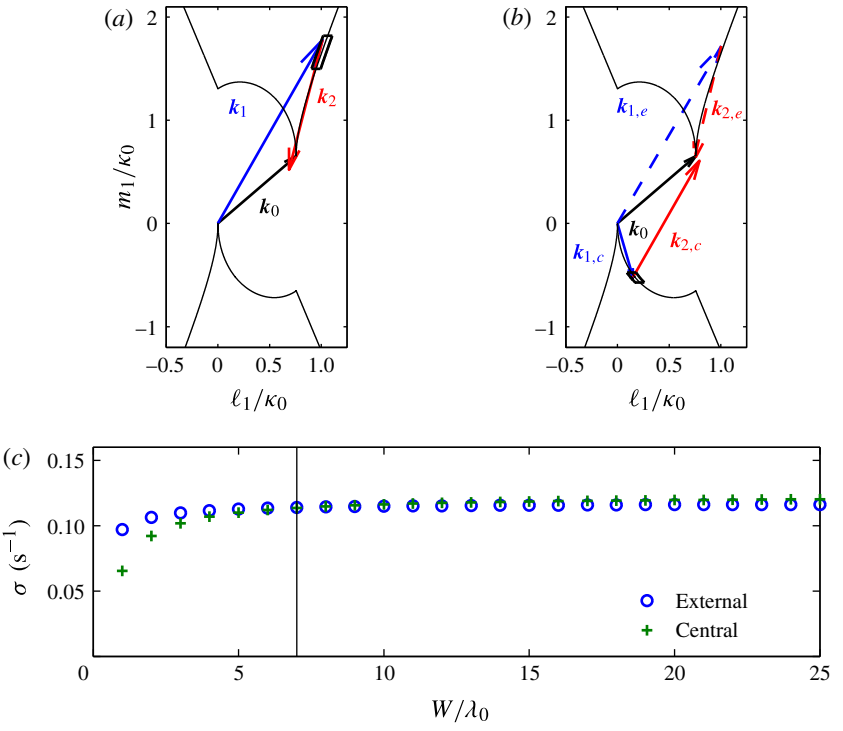


FIGURE 4. (Colour online) (*a*) The three arrows are the measurements of the three wavevectors for the numerical case $W = 3\lambda_0$. (*b*) The five arrows are the measurements of the wavevectors for the numerical case $W = 20\lambda_0$. In (*a*) and (*b*), the dark solid line represents the theoretical resonance loci for the secondary wavevector $\boldsymbol{k}_1$ for a given $\boldsymbol{k}_0$ and the rectangles represent the most unstable mode for the present finite-width model. (*c*) Evolution of the growth rate computed from (3.7) as a function of the width of the beam, computed using the finite-size model. The transition between the external and central triad configurations is obtained around $W = 7\lambda_0$ (vertical line).

right order of magnitude when compared with numerical values, 0.5 day^{-1} (Gerkema *et al.* 2006) or 0.66 day^{-1} (Gayen & Sarkar 2013), and with oceanic measurements, from 0.2 to 0.5 day^{-1} (McKinnon *et al.* 2012). In contrast for a larger beam, the instability enables transfer to both larger and smaller scales ($\kappa_1 = 1.7\kappa_0$, $\kappa_2 = 0.7\kappa_0$) which corresponds to the infinitely wide theory prediction.

This transition depends on the amplitude of the stream function Ψ_0. For example, for Ψ_0 three times larger, the transition is obtained for $W = 0.55\lambda_0$. In contrast, for Ψ_0 three times smaller, the transition is obtained for $W = 4.5\lambda_0$. Thus, the transition between the two behaviours appears for W close to the typical width of an oceanic beam. Consequently, the finite width of the beam can have a notable impact on the selection of the triad in oceanic cases and provides an explanation for the predominance of energy transfer to smaller scales for oceanic narrow beams.

6. Conclusion

We have shown theoretically, numerically and experimentally that the width of the internal wave beam is a key element in PSI. This feature had been totally overlooked

https://doi.org/10.1017/jfm.2014.550 Published online by Cambridge University Press

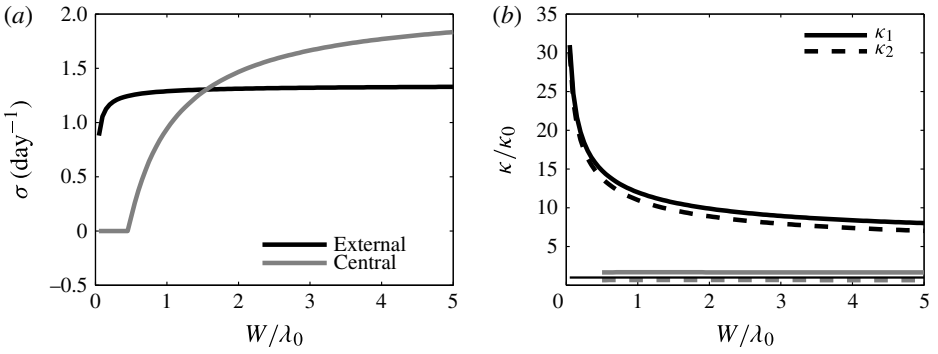


FIGURE 5. (*a*) Evolution of the growth rate computed from (3.7) as a function of the width of the beam, computed using the finite-size model in an oceanic case ($N = 1.12 \times 10^{-3}$ rad s^{-1}, $\omega_0/N = 0.125$, $\lambda_0 = 100$ m, $f = 0$). The transition between the external and central triad configurations is obtained around $W = 1.5\lambda_0$. (*b*) Evolution of the modulus of the secondary wavevectors for the external case in black and the central case in grey as a function of the width of the beam. The horizontal thin black line represents $\kappa/\kappa_0 = 1$.

previously, despite its dramatic consequences on the triad selection mechanism. The subharmonic plane waves that are theoretically unstable can only extract energy from the primary wave if they do not leave the primary beam too quickly. This finite-width mechanism has two opposite consequences on the wave energy dissipation: it introduces a PSI threshold (reducing transfer and therefore dissipation), but when PSI is present it enhances the transfer towards small wavelengths, more affected by dissipation. A complete theoretical study of the impact of the envelope on the PSI will be a timely achievement. We are aware of a recent work about the weakly nonlinear asymptotic analysis of the problem by Karimi & Akylas (2014).

It has not escaped our attention that the Coriolis force will significantly modify the prediction. Indeed, the group velocity for inertia–gravity waves, which is proportional to $\sqrt{(\omega^2 - f^2) \cdot (N^2 - \omega^2)}/(\omega\kappa)$, decreases with the Coriolis parameter f (Gill 1982). The rotation reducing the ability of subharmonic waves to escape, it seriously reinforces the instability. At the critical latitude, the group velocity vanishing, one should even recover the theoretical prediction for plane waves.

Finally, from a more fundamental point of view, such a mechanism modifies significantly the transfer of energy between scales and must be taken into account in all analyses (Caillol & Zeitlin 2000; Lvov *et al.* 2010; Lvov, Polzin & Yokoyama 2012) of wave turbulence, in which infinitely wide plane waves are until now the common theoretical objects, but not appropriate for careful predictions.

Acknowledgements

We thank P. Meunier for insightful discussions. This work has been partially supported by the ONLITUR grant (ANR-2011-BS04-006-01) and achieved thanks to the resources of PSMN from ENS de Lyon. M.L.B. acknowledges financial support from the European Commission, Research Executive Agency, Marie Curie Actions (project FP7-PEOPLE-2011-IOF-298238).

https://doi.org/10.1017/jfm.2014.550 Published online by Cambridge University Press

Appendix A. Is there an amplitude threshold in resonant triadic instability for an infinitely wide wave beam?

The expression (3.7) shows that, to obtain a strictly positive growth rate, the amplitude of the stream function has to be larger than

$$|\Psi_s(l_1, m_1)| = \frac{\nu}{2}\sqrt{\frac{\kappa_1^2\kappa_2^2}{I_1 I_2}}, \tag{A 1}$$

with I_1 and I_2 defined in (3.6). This expression has already been reported in Koudella & Staquet (2006) and Bourget *et al.* (2013) with minor typos in the latter case. What has been overlooked is that the PSI threshold is the global minimum of this function (A 1) of several variables.

In this appendix, we study the behaviour of Ψ_s when $\boldsymbol{k}_1$ tends to $\boldsymbol{k}_0$, which is the most unstable case for small values of the amplitude. In this case, we assume

$$\ell_1 = \ell_0(1 + \mu_0\epsilon^\alpha), \tag{A 2}$$

$$m_1 = m_0(1 + \epsilon), \tag{A 3}$$

with $\epsilon = o(1)$, $\alpha \geqslant 1$ and ϵ and μ_0 are positive.

Using the temporal and spatial resonance conditions and the dispersion relation of internal waves, we obtain the relation

$$\frac{m_0^6}{\kappa_0^6}\left(\epsilon^4 - 2\mu_0\epsilon^{3+\alpha} + o(\epsilon^{2\alpha})\right) = \mu_0^2\epsilon^{2\alpha}. \tag{A 4}$$

To solve this equation, there are *a priori* two different solutions for α:

(*a*) $3 + \alpha = 2\alpha$ leading to $\alpha = 3$; however, this value makes it possible to balance terms at order ϵ^6 but not the lower-order term ϵ^4, so this value $\alpha = 3$ is therefore not acceptable;

(*b*) $4 = 2\alpha$ leading to $\alpha = 2$; in that case, the lowest order terms can be balanced and one obtains $\mu_0 = (m_0/\kappa_0)^3$.

Finally, we obtain

$$\ell_1 = \ell_0(1 + \mu_0\epsilon^2) \quad \text{and} \quad \ell_2 = -\mu_0\ell_0\epsilon^2 \tag{A 5a,b}$$

$$m_1 = m_0(1 + \epsilon) \quad \text{and} \quad m_2 = -m_0\epsilon. \tag{A 6a,b}$$

With these relations, it can be shown that

$$I_1 = -\ell_0 m_0\epsilon + o(\epsilon) \quad \text{and} \quad I_2 = -\ell_0 m_0 + o(1), \tag{A 7a,b}$$

which means that

$$|\Psi_s| = \frac{\nu}{2}\frac{N}{\omega_0}\sqrt{\epsilon} + o(\epsilon^{1/2}). \tag{A 8}$$

Therefore, the minimum of the positive expression (A 1) is zero. Consequently, there is no threshold for an infinitely wide wave beam.

https://doi.org/10.1017/jfm.2014.550 Published online by Cambridge University Press

REFERENCES

BENIELLI, D. & SOMMERIA, J. 1998 Excitation and breaking of internal gravity waves by parametric instability. *J. Fluid Mech.* **374**, 117–144.

BOURGET, B., DAUXOIS, T., JOUBAUD, S. & ODIER, P. 2013 Experimental study of parametric subharmonic instability for internal plane waves. *J. Fluid Mech.* **723**, 1–20.

CAILLOL, P. & ZEITLIN, V. 2000 Kinetic equations and stationary energy spectra of weakly nonlinear internal gravity waves. *Dyn. Atmos. Oceans* **32** (2), 81–112.

CLARK, H. A. & SUTHERLAND, B. R. 2010 Generation, propagation and breaking of an internal wave beam. *Phys. Fluids* **22**, 076601.

DALZIEL, S. B., HUGHES, G. O. & SUTHERLAND, B. R. 2000 Whole-field density measurements by 'synthetic schlieren'. *Exp. Fluids* **28** (4), 322–335.

DEWAN, E. M., PICARD, R. H., O'NEIL, R. R., GARDINER, H. A., GIBSON, J., MILL, J. D., RICHARDS, E., KENDRA, M. & GALLERY, W. O. 1998 MSX satellite-observations of thunderstorm-generated gravity-waves in mid-wave infrared images of the upper-stratosphere. *Geophys. Res. Lett.* **25**, 939–942.

GAYEN, B. & SARKAR, S. 2013 Degradation of an internal wave beam by parametric subharmonic instability in an upper ocean pycnocline. *J. Geophys. Res.* **118** (9), 4689–4698.

GERKEMA, T., STAQUET, C. & BOURUET-AUBERTOT, P. 2006 Decay of semi-diurnal internal-tide beams due to subharmonic resonance. *Geophys. Res. Lett.* **33**, L08604.

GILL, A. E. 1982 *Atmosphere–Ocean Dynamics,* vol. 30. Academic Press.

GOSTIAUX, L. & DAUXOIS, T. 2007 Laboratory experiments on the generation of internal tidal beams over steep slopes. *Phys. Fluids* **19**, 028102.

GOSTIAUX, L., DIDELLE, H., MERCIER, S. & DAUXOIS, T. 2007 A novel internal waves generator. *Exp. Fluids* **42** (1), 123–130.

HINDMARSH, A. C., BROWN, P. N., GRANT, K. E., LEE, S. L., SERBAN, R., SHUMAKER, D. E. & WOODWARD, C. S. 2005 SUNDIALS: suite of nonlinear and differential/algebraic equation solvers. *ACM Trans. Math. Softw.* **31**, 363–396.

KARIMI, H. H. & AKYLAS, T. R. 2014 Parametric subharmonic instability of internal waves: locally confined beams versus monochromatic wavetrains. *J. Fluid Mech.* **757**, 381–402.

KOUDELLA, C. R. & STAQUET, C. 2006 Instability mechanisms of a two-dimensional progressive internal gravity wave. *J. Fluid Mech.* **548**, 165–196.

LIEN, R. C. & GREGG, M. C. 2001 Observations of turbulence in a tidal beam and across a coastal ridge. *J. Geophys. Res.* **106**, 4575–4591.

LVOV, Y. V., POLZIN, K. L., TABAK, E. G. & YOKOYAMA, N. 2010 Oceanic internal-wavefield: theory of scale-invariant spectra. *J. Phys. Oceanogr.* **40**, 2605–2623.

LVOV, Y. V., POLZIN, K. L. & YOKOYAMA, N. 2012 Resonant and near-resonant internal wave interactions. *J. Phys. Oceanogr.* **40**, 669–691.

MCEWAN, A. D. & PLUMB, R. A. 1977 Off-resonant amplification of finite internal wave packets. *Dyn. Atmos. Oceans* **2** (1), 83–105.

MCKINNON, J. A., ALFORD, M. H., SUN, O., PINKEL, R., ZHAO, Z. & KLYMAK, J. 2012 Parametric subharmonic instability of the internal tide at 29°N. *Am. Meteorol. Soc.* **43** (1), 17–28.

MERCIER, M. J., GARNIER, N. B. & DAUXOIS, T. 2008 Reflection and diffraction of internal waves analyzed with the Hilbert transform. *Phys. Fluids* **20** (8), 086601.

MERCIER, M. J., MARTINAND, D., MATHUR, M., GOSTIAUX, L., PEACOCK, T. & DAUXOIS, T. 2010 New wave generation. *J. Fluid Mech.* **657**, 308–334.

SUN, O. & PINKEL, R. 2013 Subharmonic energy transfer from the semi-diurnal internal tide to near-diurnal motions over Kaena Ridge, Hawaï. *J. Phys. Oceanogr.* **43**, 766–789.

SUTHERLAND, B. R. 2013 The wave instability pathway to turbulence. *J. Fluid Mech.* **724**, 1–4.

SUTHERLAND, B. R., DALZIEL, S. B., HUGHES, G. O. & LINDEN, P. F. 1999 Visualization and measurement of internal waves by 'synthetic schlieren'. Part I. Vertically oscillating cylinder. *J. Fluid Mech.* **390**, 93–126.

https://doi.org/10.1017/jfm.2014.550 Published online by Cambridge University Press